Available online at www.sciencedirect.com
ScienceDirect
Journal of the European Ceramic Society 30 (2010) 2313–2321
www.elsevier.com/locate/jeurceramsoc

Plasma wind tunnel testing of ultra-high temperature ZrB_2–SiC composites under hypersonic re-entry conditions

Frederic Monteverde [a,*], Raffaele Savino [b], Mario De Stefano Fumo [b], Andrea Di Maso [b]

[a] *Institute of Science and Technology for Ceramics, Via Granarolo 64, 48018 Faenza, Italy*
[b] *Department of Aerospace Engineering, University of Naples "Federico II", P.le Tecchio 80, 80125 Naples, Italy*

Available online 20 February 2010

Abstract

The resistance to oxidation and optical properties of a hot-pressed ZrB_2–SiC composite were studied under aero-thermal heating in a strongly dissociated flow that simulates hypersonic re-entry conditions. Ultra-high temperature ceramic models with a blunt or sharp profile were exposed to high enthalpy flows of an N_2/O_2 gas mixture up to 10 MJ/kg for a full duration of 540 s, the surface temperatures approaching 2100 K. Stagnation-point temperatures as well as spectral emissivities were directly determined using an optical pyrometer. Microstructural features of the oxidized layers were correlated to optical properties through computational fluid dynamics calculations which allow for numerical rebuilding of key parameters like surface temperatures, wall heat fluxes, shear stresses or concentrations of the species composing the reacting gas mixture. Gradients of temperature on the surfaces facing the hot gas flow established different boundary conditions that led to the formation and evolution of distinct layered oxide scales.

Keywords: Hot-pressing; Borides; Electron microscopy; Thermal properties; Arc-jet testing

1. Introduction

Ultra-high temperature ceramics (UHTCs) containing transition metal borides are under intensive analysis for applications in extreme environments,[1–3] where high-temperature aerospace applications on hypersonic vehicles have been the most investigated.

UHTC composites based on ZrB_2 and HfB_2, in combination with silica formers such as SiC or metal silicides like $MoSi_2$, $TaSi_2$, or $HfSi_2$, are particularly attractive for leading edge and control surface components on hypersonic vehicles.[4–6] To reduce aerodynamic drag and thus enhance lift-to-drag and maneuverability, hypersonic vehicles require sharp leading edged profiles with radii of curvature on the order of a few millimeters. This configuration conversely gives rise to harsher heat fluxes at the stagnation point, on the order of some MW/m^2, that in turn lead to generated surface temperatures exceeding the usage temperature of conventional aerospace materials, such as carbon fiber reinforced SiC matrix composites.[7] The utilization of materials with high thermal conductivities at high temperatures, like ZrB_2 and HfB_2, is an option that favors a faster spatial redistribution of the excess heat, and therefore may ensure performance advantages for sharp leading-edge components for which drawing heat away from the stagnation points is essential. Lower manufacturing costs and reduced density make ZrB_2-based composites more attractive for aerospace applications, compared to their HfB_2-based analogs. In spite of the high melting points for ZrB_2 and its metal oxide ZrO_2, both above 2800 K, the technological solution is still challenged by the adverse consequences of oxidation and levels of fracture toughness unable to prevent cracking during rapid thermal transients. The introduction of SiC in combination with ZrB_2 has demonstrated enhanced resistance to oxidation, fracture toughness and thermal shock resistance.[8,9] A large body of research has also been addressing the oxidation behavior of ZrB_2 and its composites using conventional air-furnace environments.[10–13] In high-temperature oxidizing environments, ZrB_2–SiC composites react with oxygen through the net parallel reactions:

$$ZrB_2 + 5/2O_2 = ZrO_2 + B_2O_3 \quad (1)$$

$$SiC + 3/2O_2 = SiO_2 + CO(g) \quad (2)$$

that yield oxide by-products like zirconia (ZrO_2), boron oxide (B_2O_3) and silica (SiO_2). Boron oxide, which melts at 450 °C,

* Corresponding author. Tel.: +39 0546 699758; fax: +39 0546 46381.
E-mail address: frederic.monteverde@istec.cnr.it (F. Monteverde).

0955-2219/$ – see front matter © 2010 Elsevier Ltd. All rights reserved.
doi:10.1016/j.jeurceramsoc.2010.01.029

promptly mixes with SiO_2 for temperatures above 1200 °C to form a borosilicate glass that spreads over and seals the external surfaces. The large volume increase upon oxidation of the bulk material due to the formation of solid zirconia was proposed as the driving force for the upward transportation of the fluid borosilicate glass.[10] With increasing testing temperature, the B_2O_3 component of the borosilicate glass possesses an unusually high vapour pressure that leads it to evaporate preferentially from the glassy phase leaving behind a boron-deficient silica layer. As the silica-rich layer thickens, it slows down the inward diffusion of oxygen to the pristine material below, limiting oxidation and lowering the oxygen partial pressure in the reaction zone.[14] At sufficiently low oxygen pressures,[15] the oxidation of ZrB_2 becomes negligible and the oxidation of silicon carbide becomes "active," proceeding through the main reaction:

$$SiC + O_2(g) = SiO(g) + CO(g) \quad (3)$$

In air-furnace studies of ZrB_2–SiC composites typically have ranged from 1273 to 1873 K, and more rarely up to 2173 K,[12,13] at atmospheric pressures. When oxidized, this group of UHTC ZrB_2-composites (10–30% SiC) forms a multilayer oxide scale with an outermost dense silica-rich glassy layer decorated with ZrO_2 crystallites and an inner SiC-depleted diboride layer, separated at times by an additional layer based on ZrO_2 crystals embedded in a silica-rich glassy network. Test conditions such as temperature and time, or type of secondary phases (coupled to initial sintering additives) affect compositions and relative thicknesses of the reaction layers.[16–18] Oxidation rates, most often quantified by monitoring the mass change of the specimens in a thermal gravimetric analyzer working at atmospheric pressure, are consistent with diffusion-limited oxidation (i.e., parabolic kinetics). Oxidation under lower total pressures and higher temperatures can result in evaporation of the SiO_2 in addition to the B_2O_3, leaving behind a single outer layer of porous ZrO_2 and resulting in rapid, linear oxidation kinetics.[15]

In contrast to conventional high-temperature air-furnace experiments where the gas environment can be assumed in thermal equilibrium with the test specimen, arc-jet wind tunnels generate high-enthalpy and strongly dissociated gas flows that more actively reproduce the aero-heating expected in service on hypersonic vehicles. Such an aero-thermal environment involves not only large temperature gradients between the specimen surfaces and the boundary layer and shock layer edges, but also an energized reactive gas mixture composed of ions, atoms, and molecules in highly energetic states whose vibrational temperature may exceed 10,000 K. The shocked gas will undergo thermochemical relaxation as it nears the colder surface, but typically will not reach chemical equilibrium at the temperature of the surface. One implication of this thermochemical non-equilibrium is that UHTC materials on leading-edge surfaces may interact with significant concentrations of dissociated gas species, whose reactivities often trigger new exothermic reactions. The validation of this class of materials to operate in such sustained environments requires a test campaign in ground-simulated (hypersonic) re-entry conditions, using facilities capable of simulating at least the representative total enthalpy, pressure and heat flux, even though they cannot simultaneously simulate the fully representative flight envelope in terms of Mach and Reynolds numbers.[19] A restricted number of available facilities in conjunction with expensive testing costs still limits the execution of dedicated studies.

In this paper, the oxidation behavior of a hot-pressed ZrB_2–SiC composite shaped as a blunt hemisphere or sharp cone was investigated using a plasma wind tunnel facility which simulates hypersonic re-entry conditions. The microstructure and composition of the resulting oxide layers were characterized and discussed. Surface temperatures and spectral emissivities were directly measured, and input in computational fluid dynamics (CFD) simulations to rebuild the aero-heating environment.

2. Materials

The ZrB_2 + 20 vol% SiC UHTC composite was prepared from commercially available powders supplied by H.C. Starck (ZrB_2 grade B, β-SiC BF12). An amount of 3 vol% Si_3N_4 supplied by Bayer (type Baysinid) was added into the base mixture as a sintering aid. Powders in due proportions were ball-milled for 24 h in a polyethylene bottle using silicon nitride media and absolute ethyl alcohol, dried by a rotary evaporator, and sieved (250 μm mesh size). The dried powder was cold compacted into a pellet (44 mm diameter) using an uniaxial press and then positioned inside a graphite mould whose internal walls were lined with BN-coated graphite foil. Hot-pressing of the powder pellet was carried out under rough vacuum (0.5–1 mbar) heating up to 2173 K (about 20 K/min heating rate and 30 MPa of applied pressure). The isothermal hold at 2173 K lasted about 10 min. At the end of the hold, the applied pressure was released and the hot press was cooled to room temperature. After removal from the dies, the hot-pressed compact was about 20 mm thick. The ceramic samples for the aero-thermodynamic study were first cut out by electrical discharge machining and then finished down to the desired dimensions using diamond-loaded tools. The base diameter is 10 mm for both the specimens, whilst the full lengths (specimen plus afterbody) are 10 mm (hemisphere) and 11 mm (cone). The curvature radii of the hemisphere and cone are, respectively, 5 and 0.5 mm.

3. Experiment

3.1. Plasma wind tunnel gallery and test conditions

The experiments were performed in the arc-jet facility "Small Planetary Entry Simulator" available at the Department of Aerospace Engineering, University of Naples "Federico II". The facility is equipped with a 80 kW plasma torch that operates with inert gases (He, N_2, Ar and their mixtures) at mass flow rates up to 5 g/s. In this case only nitrogen (80 wt%) and oxygen (20 wt%) were used. All the experiments have been carried out with a nitrogen mass flow rate of 0.8 g/s and oxygen mass flow rate of 0.2 g/s. To replicate the air composition, a percentage of 20 wt% molecular oxygen is mixed to the primary nitrogen jet into a mixing chamber after the torch. The nozzle has a throat diameter of 11 mm and an outer diameter of 22 mm. The nominal

Mach number (M), determined by the nozzle area ratio, is around 3. The ceramic model is positioned at a distance of 10 mm from the nozzle exit. Pressure transducers are installed at the nozzle exit and inside the test chamber, whilst the stagnation-point pressure at the model location is measured by a dedicated probe. The arc-power and cooling power are controlled separately, and an integrated electronic system also controls gas feed and torch current. The specific total enthalpies H_0 at the torch and nozzle exit are calculated through an energy balance on the system torch-nozzle, knowing the arc power and the cooling power. It must be pointed out that the measured total enthalpy is an average value for the flow (sometimes referred to as bulk enthalpy), and also that arc-jet facilities typically have radial gradients of the thermo-fluid-dynamic parameters, for instance the enthalpy.[20]

The test chamber is equipped with portholes and windows for optical diagnostics. Sample surface temperature is measured by a two-colour pyrometer (Infrather ISQ5, Impac Electronic GmbH, Germany) at an acquisition rate of 100 Hz. The pyrometer uses two overlapping infrared wavelength bands at 0.8–1.1 and 1–1.1 μm and measures temperatures from 1300 to 3300 K with a 1% measurement accuracy in the range 1720–3300 K. The ISQ5 pyrometer can be used both in two-colour and one-colour modes. The two-colour mode is used to measure the surface temperature, whilst the single colour mode allows to determine the emissivity once the temperature is known. The arc-jet facility presently available has no optical access in front of the model and therefore the surface model is pointed from the side of the test chamber. The measuring spot of the pyrometer is 3 mm wide and provides an average temperature of this area. For the hemispheric and conical samples the pyrometer pointed, respectively, at 50% and 80% of the radius distances from the tip.

The arc-jet wind tunnel, when used in the supersonic flow regimes, feeds a non-equilibrium flow to the shock edge (i.e. at the model's location): this might have introduced some uncertainties in the estimates of the actual gas chemical composition at the specimen surface.

3.2. Computational fluid dynamics (CFD) and thermal model

Sample temperature, gas pressure, and chemical composition of the gas mixture interacting with the UHTC model surface are key environmental parameters that influence oxidation. Surface temperature and gas pressure are determined directly, whilst the gas composition at the sample surface is computed through the numerical model based on the solution of the Favre-averaged Navier–Stokes equations for a mixture of reacting species in chemical and vibrational non-equilibrium.[21] Species viscosity, thermal conductivity, and mass diffusivity are derived from the kinetic theory of gases[22] as functions of the Lennard–Jones parameters. The solver computes the mixture viscosity and thermal conductivity with the semi-empirical Wilke's rule. The flow is considered as a mixture of five gas species: N, O, N_2, O_2, and NO. From the thermodynamic viewpoint, the system is considered a mixture of reacting ideal gases. In the present computations, the molecular species have translational and rotational modes in equilibrium, but the vibrational energy can be at different temperatures (T_V). For the chemical reactions, the Park model[23] is included, with the reaction rate constants specified by the Arrhenius law. For the vibrational and thermal relaxations, the Landau–Teller model was used,[24] with a Park correction for the higher temperatures.[25]

At solid walls, the no-slip condition is enforced by imposing the velocity components to zero. In chemically reacting flows, the mass fractions of the species are dependent variables with their transport equation. Species boundary conditions at the wall are assigned according to the behavior of the solid surface. For a fully catalytic wall, the chemical reactions are catalyzed at an infinite rate and the mass transport at the wall is limited only by diffusion, therefore the mass fractions of the dissociated species at the wall are set equal to zero. For a non-catalytic wall, the diffusive flux of atoms at the wall is set to zero. In addition, a user-defined function has been developed to simulate a wall with a finite value of surface catalycity,[26] according to Eq. (4):

$$\frac{\partial C_i}{\partial n} = \frac{C_i K_w}{D_i} \tag{4}$$

where n is the normal coordinate to the wall, C_i is the atomic mass fraction, D_i is the species diffusion coefficient and K_w is the material catalytic constant. The K_w parameter is a function of the wall material recombination coefficient γ_w ($0 \geq \gamma_w \leq 1$), of the chemical species and of the temperature, according to Eq. (5):

$$K_w = \gamma_w \sqrt{\frac{R_0 T_w}{2\pi m_i}} \tag{5}$$

R_0 is the universal gas constant, m_i is the atomic mass. In the present work the same recombination coefficient has been considered both for Oxygen and Nitrogen. The vibrational energy at the wall is set considering vibration thermodynamic equilibrium. Convective fluxes were computed according to Roe's Flux Difference Splitting scheme. Integration of the equations was implicit in the time performed, until steady state was achieved, solving the linearised system of equations by the multigrid technique. The computed surface heat flux distributions were input into the thermal analysis to rebuild the thermal history of the ceramic models under the different test conditions.

The thermal model is based on the solution of the unsteady energy equation in the solid, with the surface heat flux updated at each iteration to account for the energy re-emitted radiatively and for the changes in convective heat flux due to changes in surface temperature.[27] The computations were carried out by using the commercial FLUENT package[28] with ad hoc user-defined-functions developed in house to take into account the change of the surface temperature during the test and the radiation emitted from the surface at relatively high temperature. The thermophysical properties of the UHTC material used in this work were previously measured.[3]

3.3. Characterization of the UHTC models

UHTC models were cleaned with acetone in an ultrasonic bath, rinsed with distilled water, and dried in an oven at 373 K

Table 1
Main parameters of the experimental tests: arc power (AP), average specific total enthalpy (H_0), maximum stagnation-point pressure (P_{max}), and duration (t). The mass flow rate was 1 g/s.

	Step 1	Step 2	Step 3	Step 4	Step 5
AP (kW)	15.9	18.9	22.4	25.6	29
H_0 (MJ/kg)	4.5	5.5	7.3	8.6	10.3
P_{max} (kPa)	6.8	7.4	8.1	8.8	9.5
t (s)	80	60	60	60	230

overnight. The mass of the models was measured before and after testing (accuracy 5×10^{-2} mg). Post-test samples were prepared for microscopy by sectioning the UHTC models into two symmetrical coupons and then polished down to a 0.25 μm finish using diamond abrasives. Microstructure and composition analyses were performed by scanning electron microscopy (SEM, model S360 Leica Cambridge, UK) along with energy dispersive X-ray microanalyzer (EDX, model INCA Enegy300, Oxford Instruments, UK) on the as-exposed surfaces as well as on the polished cross-sections. A thin carbon coating was cast on the polished piece to prevent electrostatic charging of the resin (used to encase samples for polishing) during SEM observations.

4. Experimental results and discussion

4.1. Measured and derived test conditions

The experiments reported here were performed with a gas flow rate of 1 g/s, and a static chamber pressure of about 200 Pa. Average specific total enthalpy (H_0) and maximum stagnation-point pressure (P_{max}) ranged between 4.5–10.3 MJ/kg and 6.8–9.5 kPa, respectively. Peak cold-wall heat fluxes of 4.7 or 11 MW/m^2 for the hemisphere and the cone, respectively, at the maximum H_0 were calculated. Some operating conditions and derived boundary-layer-edge conditions are listed in Table 1. The ceramic models, supported on a tubular alumina holder, were moved into the hot gas flow at H_0 below 5 MJ/kg. H_0 was thus increased to the peak value of about 10.3 MJ/kg: ramp-up and final hold had a total duration of about 10 min. The experimental transient temperature profiles are given in Fig. 1 for both of the tested ceramic models. A transient thermal analysis (executed for the most severe step 5 in both models) compared the steady state temperature values with those obtained experimentally (T_{exp}). Table 2 reports the numerical averaged temperature in a 3 mm diameter spot (T_{spot}) in the same area targeted by the pyrometer. In the case of the conical model, the regions facing the hot stream just in proximity of the tip have been calculated to

Table 2
Measured temperature (T_{exp}) and numerically computed average temperature in a 3 mm diameter spot in the same area targeted by the pyrometer (T_{spot}); an emissivity of 0.6 was input for the numerical simulations. The conditions correspond to step 5 in Table 1 (steady state).

Model	T_{exp} (K)	T_{spot} (K)
Hemisphere	2053	2031
Cone	2083	2089

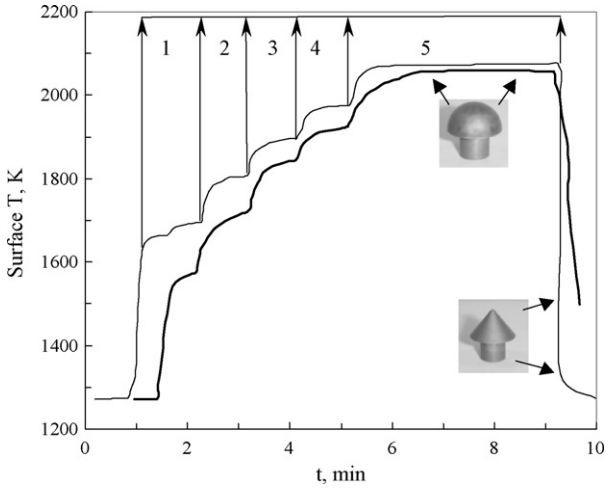

Fig. 1. Surface temperature vs. time (t) of the UHTC models; the steps for increasing H_0 are numbered (see Table 1).

reach a surface temperature of more than 2300 K (0.6 emissivity, "un-oxidized" surface). The numerical outputs T_{spot} are close to the experimental values considering an emissivity of 0.6.

As mentioned in Section 3.1, the pyrometer in both single and two-colour modes was used to evaluate temperature and spectral emissivity. In particular, in single colour mode the pyrometer allowed to determine the brightness of the sample at 1 μm wavelength (λ) and therefore the equivalent temperature (T_b) of a blackbody with the same spectral radiant energy at $\lambda = 1$ μm. Once the real surface temperature (T_{exp}) was evaluated with the two-colour mode, the coefficient of spectral emissivity ε_λ was obtained using the following equation:

$$\ln \varepsilon_\lambda = \left(\frac{c_2}{\lambda}\right)\left(\frac{1}{T_{exp}} - \frac{1}{T_b}\right) \quad (6)$$

where c_2 is the Planck radiation constant.

Spectral emissivity (ε_λ) values at different temperatures are shown in Table 3. The reported ε_λ data of the UHTC specimen appear to change as its surface progressively interacts during exposure to the hot stream, changing the chemical nature of the surface under oxidation. In comparison to experiments performed in high enthalpy subsonic flow conditions ($\varepsilon_{\lambda,1\,\mu m} = 0.9$[3]), spectral emissivity was lower at the highest temperature (Table 3). This can be explained by the different dominant chemical composition of the reaction products formed at surface during oxidation. Cross-sectioned

Table 3
Measured spectral emissivity at 1 μm ($\varepsilon_{\lambda,\ 1\,\mu m}$) at different temperature (T). Temperature values were selected increasing the arc-power, according to Table 1.

T (K)	$\varepsilon_{\lambda,\ 1\,\mu m}$	
	Cone	Hemisphere
1600	0.8	0.78
1700	0.78	0.77
1780	0.77	0.75
1865	0.75	0.74
2025	0.63	0.66

hemispherical specimens examined after exposure to high enthalpy arc-jet subsonic flow revealed the presence of a more compact external silica layer[3] in comparison to the present supersonic arc-jet experiments. However, the cross-sectioned polished specimens of the present study showed a prevailing concentration of zirconia composing the external oxide layer which is responsible of a lower emissivity.

These results show that the flow behavior may influence surface oxidation. One direct consequence of a reduced spectral emissivity of the surface is that the specimen reaches a stagnation-point temperature comparable to that achieved in a subsonic flow[3] even though H_0 is half of that applied in high pressure tests (i.e. 20 MJ/kg). The knowledge of these parameters is essential to correlate the extent of the oxidation by changing testing conditions. In the present case, the use of two surface geometries in the same flowfield has led to dissimilar boundary conditions upon the surfaces impinged by the hot stream. Whereas stagnation-point surface temperature and gas pressure were determined directly, the gas composition at the sample surface was computed through the numerical model based on the solution of the Favre-averaged Navier–Stokes equations for a mixture of reacting species in chemical and vibrational non-equilibrium. A more detailed description is reported in the next sections.

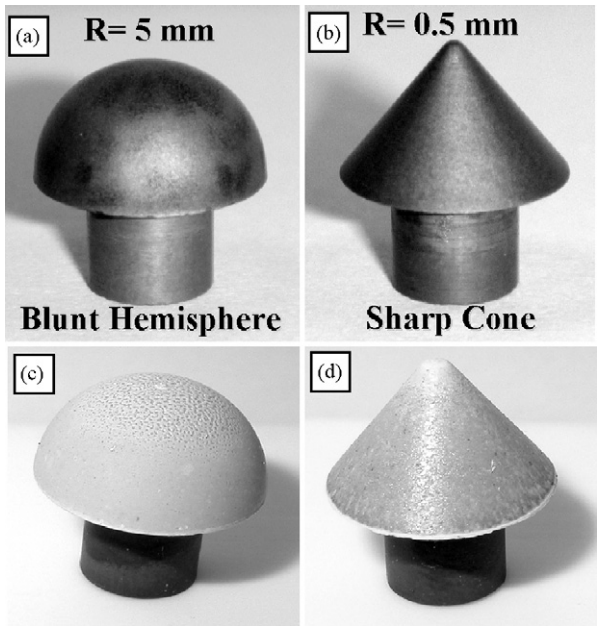

Fig. 2. Visual appearance of the ceramic models before (a and b) and after testing (c and d); *R*: radius of curvature.

4.2. Formation and morphology of the oxidized layers

Both the UHTC specimens survived the arc-jet exposure without any optical evidence of mechanical failure (Fig. 2). Mass changes turned into net losses of 0.5 and 0.6% for the blunt hemisphere and the sharp cone, respectively. The post-test inspection at a macroscale level revealed a rather smooth contour of the oxidized surface and a whitish coloration. In the case of the cone this whitish colour was concentrated at the tip.

At higher magnifications, the oxidized surfaces appear more inhomogeneous, and mostly covered by a glassy coating. The major contribution to the varying surface roughness arises from the presence of craters, which are presently interpreted as the signature of the evolution of gases during exposure.

The craters were differentiated in size and shape depending on their position with respect to the stagnation point (Fig. 3). The distribution of the shear stresses (Fig. 4), computed at steady state for the same conditions reported in Table 2 (step 5) correlates well with the evolution/bursting of bubbles. In fact, a localized increase in the shear stress favors an anticipated explosion of gas bubbles (see small sized craters close to the tip in Fig. 3), whilst in the regions less perturbated by the shear stresses the bubbles may evolve and grow in size in a relatively longer time (before bursting). Moving towards the colder regions of the ceramic models, the simultaneous reduction of the surface temperature (Fig. 5) and shear stresses lead the bubbles to form and eventually burst much less frequently. Looking into the cross-sectional surfaces by SEM-EDX, an interesting variety of oxidized sub-layers extending below the outermost glassy layer was revealed. The morphologies of the oxidized layers differ significantly, depending not only on the initial model's geometry, but also on the position with respect to the stagnation point. The SEM images presented in Fig. 6, though necessarily selective, are representative of the thicknesses of the oxide layers formed. Based on the SEM-EDX observations of the layered oxide structures, an appreciable temperature gradient that developed on the exposed surfaces (Fig. 5) drove the formation of different features.

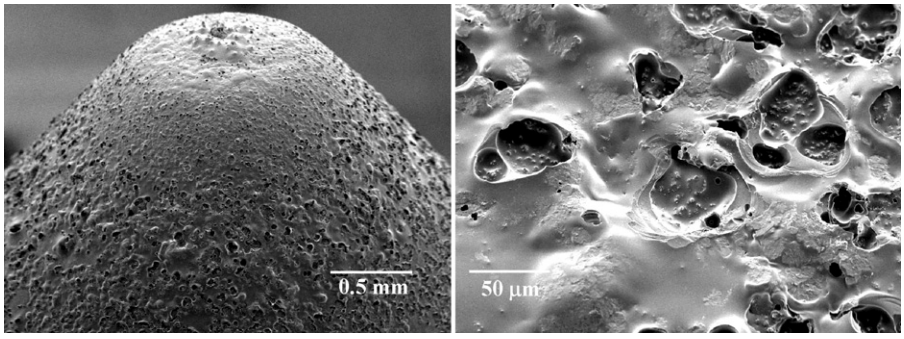

Fig. 3. Exposed surface of the sharp cone: details by SEM.

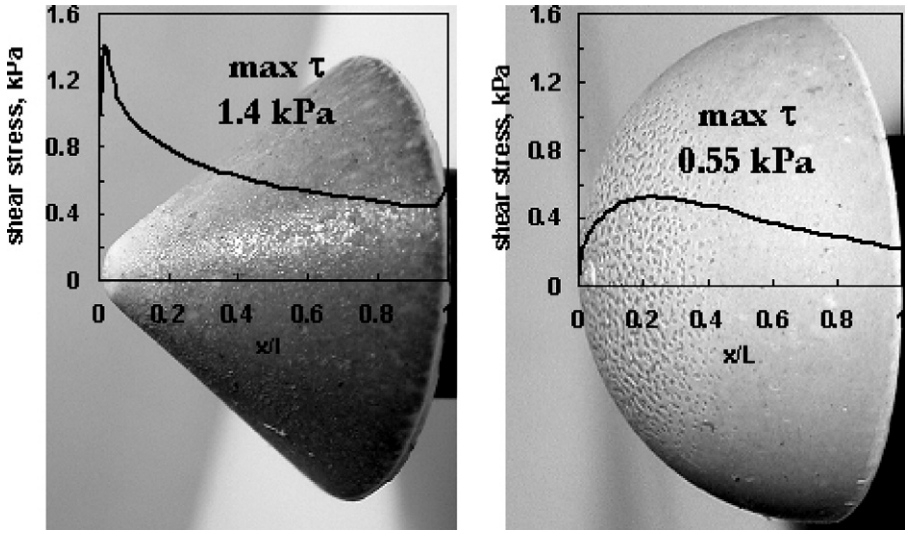

Fig. 4. Shear stress vs. curvilinear normalized coordinate (*x*/*L*).

4.2.1. Blunt hemisphere

The entire thickness of the oxidized layer varies from 150 to about 60 μm. The oxide sub-layer underlying the outermost glassy scale is characterized by a duplex morphology of the zirconia crystals: a prevailing columnar shape close to the unoxidized material, and a more globular shape nearer to the outermost surface glassy layer (Fig. 7). Also, the tiny zirconia particles which decorate the external glassy layer grow preferentially with a columnar shape. The lack of glass between adjacent columnar zirconia crystals weakens the compactness of this oxide sub-layer. On the contrary, an enrichment of glass however cements the zirconia crystals composing the upper portions of this oxide sub-layer. No obvious SiC-depleted diboride region was found, although the model's surface rose to a temperature very close to 2100 K. Looking at the interface between the bottom of the columnar-type zirconia sub-scale and the underlying unoxidized bulk in finer details, widespread microposity is present. This porosity is believed to have nucleated during exposure to the hot plasma, when an incipient inner depletion of SiC very likely began to take place due to its active oxidation. Raising the temperature, oxidation proceeded so fast that the former SiC-depleted diboride matrix readily oxidized into columnar zirconia particles, whose peculiar shape suggests the outward escape of gas species and/or transportation to the surface layer by liquid convection.[13] The inner oxidation of ZrB_2 was accelerated by the lack of glass which did not effectively slow the inward diffusion of oxygen. This line of reasoning is under a continuing investigation (not included herein). The presence of large zirconia crystals directly facing the external ambient (Fig. 7) should also be noted. The creation of these special features is believed to have followed the bursting of bubble(s), leaving behind zirconia crystals without any protective silica glass. A locally reduced ability to dissipate heat due to a lower emissivity and (very likely) a higher catalycity in consequence of the lack of silica glass, likely gave rise to "hot-spots" where the surface temperature jumped up at sufficient levels to rapidly sinter the underlying zirconia crystallites. Localized EDX analyses confirmed the presence of only Zr and O in such exposed enlarged crystallites.

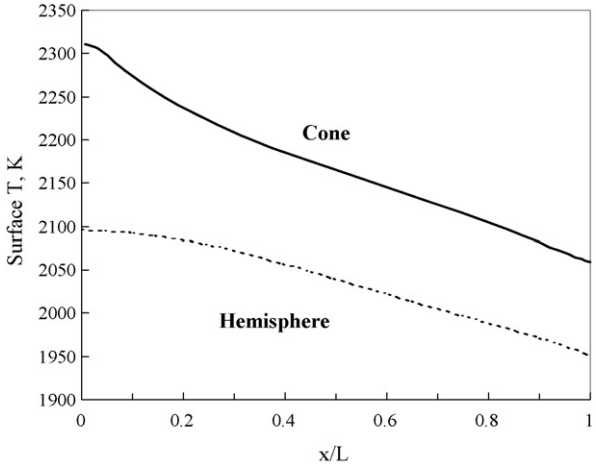

Fig. 5. Distribution of the surface temperature along the curvilinear normalized coordinate (*x*/*L*). An emissivity of 0.6 was set for the calculations.

4.2.2. Sharp cone

On the conical sample, a glassy layer covers the major part of the external surface but appears less continuous than in the hemispherical one. The entire thickness of the reaction oxide layer varies from 190 to 50 μm (Fig. 8). In contrast to the former case of the blunt hemisphere, a SiC-depleted diboride sub-region was evident, its thickness decreasing from 70 μm (at the cone tip) to a complete disappearance ($0.7 < x/L < 0.8$, x/L the normalized curvilinear coordinate of the sample). This finding corroborates the supposition that the rate of the rise in temperature is the primary boundary condition that allows (or prevents) the creation of the SiC-depleted ZrB_2 layer. The oxide sub-layer above the SiC-depleted diboride region is very close to the cone tip and has a morphology very similar to that described earlier for the blunt hemisphere, i.e. formation of both columnar and more rounded zirconia crystals. In the remaining portions of this oxide

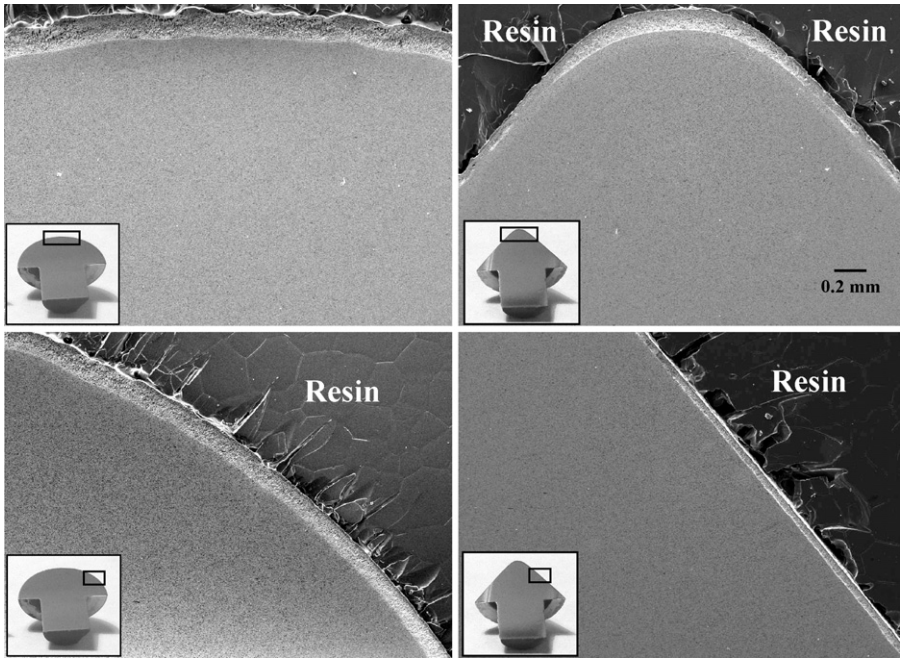

Fig. 6. Cross-sectioned and polished ceramic models (SEM micrographs at same magnification).

sub-layer (far from the apex), the typical morphology consists of globular zirconia crystals cemented within a silica-based glass.

The small zirconia particles which decorate the outermost glassy layer have crystallized preferentially with a regular round shape. Even if the density of the craters (i.e., the burst bubbles) appears more obvious in the present case (Fig. 9), the growth of large zirconia blocks directly facing the external ambient was not confirmed. The reason for this different behavior is not yet fully understood. A reasonable explanation may be that the more compact zirconia/glass mixed sub-scale better protected the inner bulk that still retains unoxidized diboride matrix in the SiC-depleted region. The in-depth active oxidation of SiC yields more silica, compared to the previous case. The more copious generation of silica assisted the preservation of a continuous network of glass which favors more oxidation protection and a mitigated exposure to the severe aero-thermal environment of the zirconia skeleton composing such oxide sub-layer. It follows that conditions of quasi-steady inward diffusion of the oxidants (i.e., O and O_2), and the outward transport of SiO and CO, are controlled by the interconnected network of silica glass. Additional investigations are in progress to determine the composition of the silica-based glass that lies upon the external face and mostly fills the gaps between the zirconia crystals constituting the oxide sub-layer.

The thin, almost continuous silica glass layer that persists over the exposed surface seems to contradict some thermodynamic assessments that set conditions for volatilization[29] On the other hand, an accurate knowledge of testing conditions in

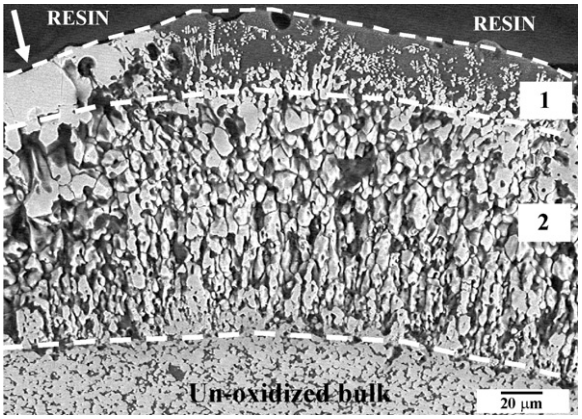

Fig. 7. Cross-sectioned and polished blunt hemisphere (tip area, back-scattered electron SEM micrograph): outermost glassy layer decorated with tiny zirconia particles (1), oxide sub-layer (2). Large zirconia crystals are indicated.

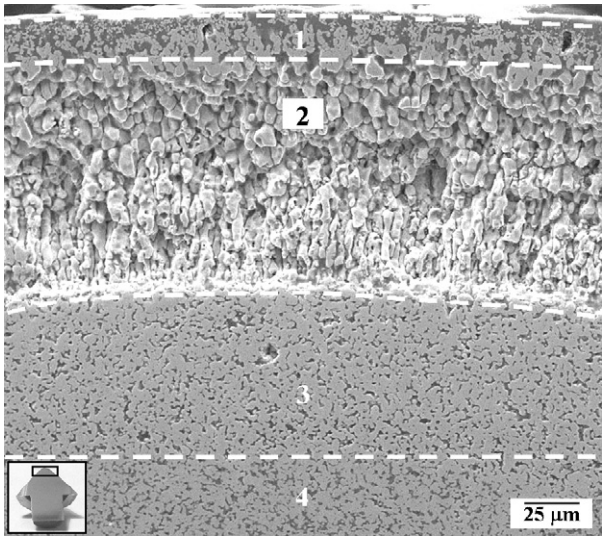

Fig. 8. Cross-sectioned and polished sharp cone (SEM micrograph): mixed zirconia/glass sub-layer (2) underlying the zirconia decorated external glassy layer (1), SiC-depleted diboride region (3) above the un-oxidized bulk (4).

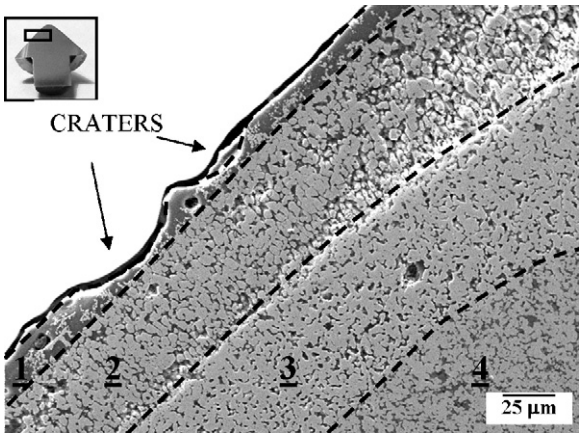

Fig. 9. Cross-sectioned and polished sharp cone (SEM micrograph): globular zirconia embedded in a glass sub-layer (2) underlying the zirconia-decorated outermost glassy layer (1), SiC-depleted diboride region (3) above the un-oxidized bulk (4).

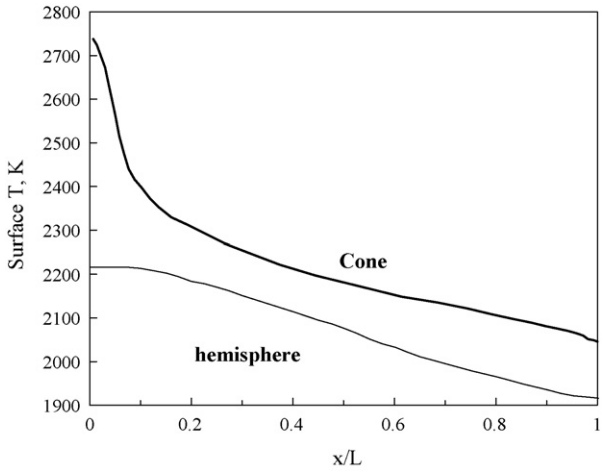

Fig. 10. Distribution of the surface temperature along the curvilinear normalized coordinate (x/L). The models have an external oxide layer 100 μm thick, 1 W/mK of thermal conductivity; a global emissivity of 0.6 was set for the calculations.

terms of temperature and partial pressure of the main gas species composing the reactive mixture (N_2, O, O_2 N, NO) is a complex task. Experimentally, the finding of such a silica glassy layer might suggest a wider stability domain of silica under dissociated oxygen and reduced pressure. Even though the duration of the tests presented herein are representative for a re-entry mission, extended exposures seem necessary to look into the effects of time over the stability domain of silica in such a special environment. In any case, the sudden drop of the surface temperature after switching-off the aero-heating makes the very fast cooling stage not effective at all to modify chemistry and microstructure of the oxidized surface. It follows that the resulting post-test microstructures, discussed in detail above, can be considered a realistic picture of the surfaces interacting with the surrounding environment.

As for the varying thickness of the SiC-depleted diboride layer, it is very likely influenced by the decreasing temperature profile along the exposed surface. Temperature aside, the oxygen partial pressure (p) is known to drive the active-to-passive oxidation transition of SiC. In the present case, the calculated patterns for p_O and p_{O2} that vary along the exposed surface do not seem to correlate with the occurrence and extent of the SiC-depleted sub-layer. More reasonably, the expected decrease of the oxygen partial pressure through the reaction layers plays a more important role in controlling the active-to-passive transition of the SiC oxidation, and therefore the transport of diffusing species in the inward and outward direction.

4.3. Surface properties

CFD simulations of fully catalytic versus non-catalytic heating of the test specimens suggest that the reacting surfaces must possess very low catalytic efficiency to explain the measured surface temperature transients. Surface characteristics, like efficiency for surface recombination (i.e catalycity) or emissivity, depend on both the chemical nature and the microstructure of the surface. Different from our previous experiments at atmospheric pressure and subsonic flow regime,[3] the spectral emissivity derived by simultaneous two- and one-colour radiometry measurements is in the range of 0.6–0.65. No data are available to date in order to compare the consistency of these results. Zhang and co-workers conducted tests in ground simulated re-entry conditions (supersonic flow) and a surface temperature of 1440–1450 °C was reached.[30] No mention was made of the spectral emissivity. The authors stressed an excellent thermal-oxidative and configurational stability, even though the scanned interval did not cover the ambitious range of values expected in an extreme hypersonic environment. In order to gain a more comprehensive understanding of the effects of the surface chemistry on the aero-heating, CFD simulations were built by modelling UHTC samples covered with a continuous oxide scale 100 μm thick (1 W/mK of thermal conductivity, typical of compounds like zirconia and silica). Plots of the distribution of the surface temperature based on the CFD simulations (Fig. 10) show a rapid increase in temperature in the near region of the sharp apex. Such evaluations experimentally are limited by the minimum finite size of the focused spot of the radiometry determinations. As expected, the sharp cone experiences a greater rise in temperature, compared to the blunt hemisphere. Interestingly, the amplified difference in the stagnation peak temperature compared to the "un-oxidized" model (Fig. 5) agrees with the evident visual dissimilarities. Persistency and homogeneity of the external glass over the surfaces of the exposed sample influence not only the catalytic surface recombination of dissociated species (O, N) but also the solubility, diffusion and in-depth reactions of oxidants, and therefore oxidation. An update of our thermal model is in progress to take into due account such variables in order to better describe the oxidation behavior of this class of materials.

5. Conclusions

ZrB_2–SiC composites are candidates for leading-edge and control surface applications on future hypersonic aerospace vehicles, for which operating temperatures approaching 2300 K,

or even higher, in the presence of partially dissociated oxygen are expected. This study tested samples with sharp and blunt geometries in simulated hypersonic re-entry conditions using an arc-jet plasma wind tunnel. Under the conditions of this study, measured surface temperatures near 2100 K resulted in (calculated) cold-wall heat fluxes up to 11 MW/m^2. Changes in specimen dimensions and mass were minimal. The exposures resulted in oxidation of the specimen's surfaces, which produced an outer layer of silica-based glass and an underlying layer of mixed ZrO_2/SiO_2. The boundary conditions resulted in the development of both columnar and more rounded zirconia crystals. The measured spectral emissivity (at 1 μm) had values in the range of 0.6–0.65 for temperatures above 2000 K. The persistency of a residual external silica glassy layer suggested an extension of the stability domain in such harsh conditions of temperature and pressure when oxygen is dissociated. The occurrence of graded temperature contours along the model surface was recognized as the key parameter controlling formation, extent and chemistry of the resulting oxide layered structures. The obvious formation of SiC-depleted diboride-based regions took place only in the case of the sharp cone, where the measured stagnation-point temperatures reached values of 2100 K. CFD simulations, which assumed an un-oxidized status of the exposed surface, estimated peak values close to 2300 K (cone) and 2100 K (hemisphere). Future studies are planned to update a thermal model which takes into account effects of the changing microstructure (i.e., growth of a thermally insulating scale) on the optical characteristics of this class of materials.

Acknowledgement

The authors thank Mr. D. Dalle Fabbriche (ISTEC-CNR) for technical assistance in the hot-pressing.

References

1. Marschall J, Pejakovic DA, Fahrenholtz WG, Hilmas GE, Zhu S, Ridge J, et al. Oxidation of ZrB_2–SiC ultrahigh-temperature ceramic composites in dissociated air. *J Thermophys Heat Transfer* 2009;**23**(2):267–78.
2. Zhang X, Weng L, Han J, Meng S, Han W, Preparation. thermal ablation behavior of HfB_2–SiC based ultra-high-temperature ceramics under severe heat conditions. *Int J Appl Ceram Technol* 2009;**6**(2):134–44.
3. Monteverde F, Savino R. Stability of ultra-high-temperature ZrB_2–SiC ceramics under simulated atmospheric re-entry conditions. *J Eur Ceram Soc* 2007;**27**:4797–805.
4. Monteverde F. Ultra-high temperature HfB_2–SiC ceramics consolidated by hot-pressing and spark plasma sintering. *J Alloys Compd* 2007;**428/1-2**:197–205.
5. Monteverde F. Hot pressing of hafnium diboride aided by different sinter additives. *J Mater Sci* 2008;**43**:1002–7.
6. Sciti D, Monteverde F, Guicciardi S, Pezzotti G, Bellosi A. Microstructure and mechanical properties of ZrB_2–$MoSi_2$ ceramic composites produced by different sintering techniques. *Mater Sci Eng A* 2006;**434**:303–9.
7. Tang S, Deng J, Wang S, Liu W. Comparison of thermal and ablation behavior of C/SiC composites and C/ZrB_2–SiC composites. *Corr Sci* 2009;**51**:54–61.
8. Monteverde F. The addition of SiC particles into a $MoSi_2$-doped ZrB_2 matrix: effects on densification, microstructure and thermo-physical properties. *Mater Chem Phys* 2009;**113**:626–33.
9. Zimmermann JW, Hilmas GE, Fahrenholtz WG. Thermal shock resistance of ZrB_2 and ZrB_2–30% SiC. *Mater Chem Phys* 2008;**112**(1):140–5.
10. Karlsdottir SN, Halloran JW. Formation of oxide films on ZrB_2–15 vol%SiC composites during oxidation: evolution with time and temperature. *J Am Ceram Soc* 2009;**92**(6):1328–32.
11. Carney CM, Mogilvesky P, Parthasarathy TA. Oxidation behaviour of zirconium diboride silicon carbide produced by the spark plasma sintering method. *J Am Ceram Soc* 2009;**92**(9):2046–52.
12. Han W-B, Hu P, Zhang X-H, Han J-C, Meng S-H. High-temperature oxidation at 1900 °C of ZrB_2–*x*SiC ultrahigh-temperature ceramic composites. *J Am Ceram Soc* 2008;**91**(10):3328–34.
13. Zhang X-H, Hu P, Han J-C. Structure evolution of ZrB_2–SiC during oxidation in air. *J Mater Res* 2008;**23**(7):1961–72.
14. Rezaie A, Fahrenholtz WG, Hilmas GE. Evolution of structure during the oxidation of zirconium diboride–silicon carbide in air up to 1500 °C. *J Eur Ceram Soc* 2007;**27**:2495–501.
15. Rezaie A, Fahrenholtz WG, Hilmas GE. Oxidation of zirconium diboride-silicon carbide at 1500 °C at a low partial pressure of oxygen. *J Am Ceram Soc* 2006;**89**(10):3240–5.
16. Zhang SC, Hilmas GE, Fahrenholtz WG. Improved oxidation resistance of zirconium diboride by tungsten carbide additions. *J Am Ceram Soc* 2008;**91**(11):3530–5.
17. Talmy IG, Zaykoski JA, Opeka MM. High-temperature chemistry and oxidation of ZrB_2 ceramics containing SiC, Si_3N_4, Ta_5Si_3, and $TaSi_2$. *J Am Ceram Soc* 2008;**91**(7):2250–7.
18. Guo W-M, Zhou X-J, Zhang G-J, Kan Y-M, Li Y-G, Wang P-L. Effect of Si and Zr additions on oxidation resistance of hot-presses ZrB_2–SiC composites with polycarbosilane as a precursor at 1500 °C. *J Alloys Compd* 2009;**471**:153–6.
19. Fletcher, G. and Playez, M. *Characterization of supersonic and subsonic plasma flows, AIAA-2006-3294*, San Francisco, June 2006.
20. Grinstead, J., Driver, D. and Raiche, G. *Radial profiles of arcjet flow properties measured with laser-induced fluorescence of atomic nitrogen, AIAA-2003-0400*, January 2003.
21. Park C, Jaffe RL, Partridge H. Chemical-kinetic parameters of hyperbolic earth entry. *J Thermophys Heat Transfer* 2001;**15**(1):76–90.
22. Hirschfelder JO, Curtiss CF, Bird RB. *Molecular theory of gases and liquids*. New York: Wiley; 1954. p. 75–106.
23. Park C. Review of chemical kinetics problems for future NASA mission. Part 1: earth entries. *J of Thermophys Heat Transfer* 1993;**7**(3):385–98.
24. Millikan RC, White DR. Systematics of vibrational relaxation. *J Chem Phys* 1963;**39**(12):3209–13.
25. Park C. *Nonequilibrium hypersonic aerothermodynamics*. John Wiley & Sons; 1990.
26. Suslov, O. N. and Tirskiy, G. A. Kinetics of the recombination of nitrogen atoms on high temperature reusable surface insulation in hypersonic thermo-chemical non-equilibrium flow; 2004. In: Hunt, J. J., editor, *Proceedings of the 2nd European Symposium on Aerothermodynamics for Space Vehicles*, ESTEC, Noordwijk, The Netherlands, 21–25 November 1994, European Space Agency (ESA), Paris, 1995, p. 413–9.
27. Savino R, De Stefano Fumo M, Paterna D, Serpico M. Aerothermodynamic study of UHTC-based thermal protection systems. *Aerospace Sci Technol* 2005;**9**(2):151–60.
28. *Fluent 6.2 User's Guide*. Lebanon, NH, USA: Fluent Inc; 2004.
29. Fahrenholtz WG. Thermodynamic analysis of ZrB_2–SiC oxidation: formation of a SiC-depleted region. *J Am Ceram Soc* 2007;**90**(1):143–8.
30. Zhang X, Hu P, Han J, Meng S. Ablation behavior of ZrB_2–SiC ultra high temperature ceramics under simulated atmospheric re-entry conditions. *Comp Sci Technol* 2008;**68**(7–8):1718–26.